Research Square

Preprints are preliminary reports that have not undergone peer review.
They should not be considered conclusive, used to inform clinical practice,
or referenced by the media as validated information.

Climate-Driven Multi-Depth Soil Moisture and Irrigation Demand Projections Using Bias-Corrected CMIP6 and Machine Learning in the Amibara Agrucultural Land Near Kulfo Watershed, Ethiopia

Babur Tesfaye Yersaw

baburtesfaye@gmail.com

Arba Minch University

Demiso Daba Dugassa

Arba Minch University

Hailemariam Molla Ashagre

Arba Minch University

Demelash Wondimagegnehu Goshime

Arba Minch University

Research Article

Keywords: Climate change, CMIP6, soil moisture, machine learning, Quantile Mapping, Random Forest, irrigation requirement, explainable artificial intelligence, Kulfo watershed, Ethiopia

Posted Date: November 9th, 2026

DOI: https://doi.org/10.21203/rs.3.rs-11304054/v1

License: This work is licensed under a Creative Commons Attribution 4.0 International License.
Read Full License

Additional Declarations: No competing interests reported.

Climate-Driven Multi-Depth Soil Moisture and Irrigation Demand Projections Using Bias-Corrected CMIP6 and Machine Learning in the Amibara Agrucultural Land Near Kulfo Watershed, Ethiopia

Babur Tesfaye Yersaw[1]*, Demiso Daba Dugassa[2], Hailemariam Molla Ashagre[2], Demelash Wondimagegnehu Goshime[1]

[1] Faculty of Water Resources and Irrigation Engineering, Water Technology Institute, Arba Minch University, P.O. Box 21, Arba Minch, Ethiopia

[2] Faculty of Hydraulic and Water Resources Engineering, Water Technology Institute, Arba Minch University, Arba Minch, Ethiopia

Corresponding author: baburtesfaye@gmail.com

Highlights

- QM–RF reduced precipitation RMSE by ~18% relative to QM alone; CMCC-ESM2 ranked best for precipitation (PI = 0.83).
- CatBoost gave the strongest soil-moisture prediction at 40 cm (R^2 = 0.918; RMSE = 0.0134 cm^3/cm^3), while HistGB was best at 20 cm (R^2 = 0.956).
- Recursive hindcasting maintained skill across depths (R^2 = 0.854–0.901; best at 20 cm).
- Under SSP5-8.5, annual mean soil moisture declined by 29%, 27%, 24%, and 21% at 10, 20, 30, and 40 cm, respectively.
- Irrigation demand increased under SSP5-8.5 by 2071–2100: CWR rose from 620 to 714 mm and NIR from 210 to 301 mm.

Abstract

Climate change can modify precipitation regimes, atmospheric evaporative demand, and soil-water availability, creating substantial challenges for irrigation-dependent agriculture. Soil moisture responds differently across the soil profile, assessments based on a single soil layer may obscure important depth-dependent responses. This study developed an integrated framework combining bias-adjusted CMIP6 climate projections, machine learning, explainable artificial intelligence, recursive forecasting, and root-zone water-balance modelling to investigate climate-driven changes in multi-depth soil moisture and irrigation requirements in the Kulfo watershed, southern Ethiopia. Daily precipitation, maximum temperature, minimum temperature, and soil-moisture observations at 10, 20, 30, and 40 cm were analyzed for 2006–2014. Eighteen CMIP6 general circulation models

(GCMs) were evaluated and bias-adjusted using a two-stage Quantile Mapping–Random Forest (QM–RF) framework. The analysis separated the historical period chronologically into 2006–2010 for model development, 2011–2012 for validation and model selection, and 2013–2014 for independent testing. Five machine-learning approaches of CatBoost, Histogram-Based Gradient Boosting, LightGBM, XGBoost, and a stacking ensemble were evaluated using precipitation, temperature, antecedent precipitation, lagged temperature, and lagged soil-moisture predictors. Because lagged soil moisture is unavailable as an observed quantity during future simulation, recursive hindcasting was used to evaluate the effect of feeding model predictions back into subsequent time steps. SHapley Additive exPlanations (SHAP) were used to quantify predictor contributions to soil-moisture predictions. Following bias adjustment, CMCC-ESM2 showed the highest precipitation performance index (PI = 0.83), whereas NorESM2-MM showed the highest indices for maximum and minimum temperature (PI = 0.87 and 0.85, respectively). QM–RF reduced precipitation RMSE by 16–22% relative to QM alone (mean 18.1%). CatBoost achieved the strongest independent-test performance at 40 cm (R^2 = 0.918; RMSE = 0.0134 cm^3/cm^3), while HistGB was best at 20 cm (R^2 = 0.956). Under recursive hindcasting over the independent 2013–2014 period, R^2 values were 0.861, 0.901, 0.889, and 0.854 at 10, 20, 30, and 40 cm, respectively. Under SSP5-8.5, annual mean soil moisture was projected to decline by approximately 29%, 27%, 24%, and 21% at 10, 20, 30, and 40 cm, respectively, relative to the historical baseline. The 10th–90th percentile inter-model spread for these projections ranged from ±6% to ±11%. Crop water requirement increased from 620 mm during the historical baseline to 714 mm during 2071–2100 under SSP5-8.5, while net irrigation requirement increased from 210 to 301 mm. The combined reduction in soil-water availability and increase in crop-water demand indicates potentially greater irrigation pressure under stronger climate forcing. However, the projected changes should be interpreted as conditional scenario simulations rather than deterministic forecasts because they depend on climate-model structural uncertainty, bias-adjustment assumptions, recursive machine-learning behavior, the relatively short observational period, and crop-water-balance parameterization. Explicit representation of inter-model spread is therefore required when interpreting the magnitude and robustness of the future projections.

Keywords: Climate change; CMIP6; soil moisture; machine learning; Quantile Mapping; Random Forest; irrigation requirement; explainable artificial intelligence; Kulfo watershed; Ethiopia.

1. Introduction

Soil moisture constitutes a pivotal state variable in the terrestrial water cycle, governing the partitioning of precipitation into infiltration, runoff, and evapotranspiration, and ultimately regulating groundwater recharge and vegetation productivity (Greiser et al. 2024; Liu et al. 2026). In agricultural systems, water stored within the effective root zone directly regulates crop transpiration and thus informs irrigation scheduling, drought response, and water allocation decisions (Teshome et al. 2024; Lamichhane et al. 2025; He et al. 2026). However, soil moisture dynamics are inherently nonlinear and controlled by complex interactions among climatic variables, soil characteristics, vegetation cover, and land management practices, making accurate prediction difficult under increasing climatic variability (Li et al. 2024; Bischof et al. 2026).

Soil moisture exhibits pronounced vertical heterogeneity: near-surface layers respond rapidly to individual rainfall events and atmospheric demand, whereas deeper layers integrate infiltration, redistribution, drainage, and root-water uptake over longer timescales, resulting in greater temporal persistence and hydrological memory (Qin et al. 2023; Zhang et al. 2025). This vertical variability implies that assessments based on a single soil layer may obscure important depth-dependent responses, as shallow and deep layers may exhibit contrasting and sometimes counterintuitive reactions to the same climatic forcing (Berg and Sheffield 2018; Lai et al. 2023). Consequently, depth-resolved assessment provides more actionable information for agricultural water management than a single bulk soil-moisture indicator.

The soil moisture dynamics are particularly important in southern Ethiopia, where rainfall variability and recurrent dry periods constrain agricultural production, and where soil moisture variability strongly influences crop yield stability (Jimma et al. 2023). Agriculture in the Kulfo watershed relies partly on irrigation from surface-water and groundwater sources, yet the region is characterized by degraded lands, poor soil moisture content, and high erosion rates. As climate conditions change, fixed calendar-based irrigation becomes increasingly less responsive to shifts in rainfall timing and evaporative demand. A climate-sensitive irrigation assessment therefore requires simultaneous consideration of both crop-water demand and the availability of water within the soil profile. Climate change is expected to alter soil moisture regimes and intensify water stress in semi-arid agricultural systems (Bradford et al. 2017; Galvincio et al. 2024).

Recent studies across Ethiopia have demonstrated that bias-corrected CMIP6 projections indicate substantial increases in crop water requirements and irrigation demand, with gross irrigation demand projected to rise by 15–20% by 2100 in some regions (Legass et al. 2025a; Bokke et al. 2026a). However, such assessments have predominantly focused on highland basins (Enyew et al. 2024; Chanie 2025; Mohammed et al. 2027), leaving lowland irrigated agricultural systems largely unexplored.

Coupled Model Intercomparison Project Phase 6 (CMIP6) provides climate simulations under alternative Shared Socioeconomic Pathways (SSPs), offering improved representation of key climatic drivers such as precipitation and temperature compared to earlier model generations (Ayugi et al. 2021; Bitew and Minale 2025; Shenkut et al. 2025). Nevertheless, global climate models operate at spatial scales much coarser than individual watersheds and exhibit systematic errors in precipitation and temperature, particularly in regions with complex topography such as the Ethiopian Rift Valley (Demissie et al. 2025; Erenso et al. 2026). Statistical bias adjustment can improve the correspondence between simulated and observed climate distributions, though it cannot remove structural climate-model uncertainty or guarantee that historical relationships remain stationary in the future (Dembélé et al. 2020).

Quantile Mapping (QM) corrects distributional discrepancies, whereas a second-stage machine-learning model can represent residual systematic error not removed by QM (Babaousmail et al. 2021; Sa'adi et al. 2024). Recent applications of machine-learning-based post-processing have demonstrated meaningful reductions in bias and RMSE for climate projections (Legass et al. 2025b; Ashagre et al. 2026). A hybrid QM–RF framework that corrects both distributional and residual biases therefore offers a potentially robust approach for watershed-scale applications, provided that the correction is calibrated strictly within the historical development period and evaluated on temporally independent data.

Machine-learning methods can represent nonlinear relationships among meteorological forcing, antecedent conditions, and soil moisture (Huang et al. 2022; Li et al. 2024; Lamichhane et al. 2025). Their evaluation for time series requires strict temporal separation because random allocation of adjacent observations can allow information from later periods to enter model development and produce overly optimistic performance (Tefera et al. 2026). Chronological partitioning is therefore appropriate for forecasting applications. Moreover, when lagged soil moisture is used as a predictor, future observations are unavailable during operational forecasting

and the model must be run recursively, allowing prediction errors to propagate through successive time steps (Liu et al. 2025; Yin et al. 2026). Recursive deep-learning frameworks have recently been shown to achieve skillful forecasts of root-zone soil moisture up to four weeks in advance when combined with dynamic model forecasts (Lesinger and Tian 2025). This distinction between one-step prediction and recursive forecasting is particularly important for future climate-impact simulations, as a model may perform well when observed lagged soil moisture is supplied as an input but behave differently when its own previous predictions are recursively fed back into the model.

Explainable artificial intelligence, particularly SHapley Additive exPlanations (SHAP), provides a framework for quantifying predictor contributions to soil-moisture predictions (Yin et al. 2026). Recent applications have revealed depth-dependent shifts in meteorological controls, transitioning from short-term atmospheric drivers in shallow layers to slower-varying seasonal influences in deeper horizons (Yin et al. 2026; Demir 2026; Dong et al. 2026). Transformer-SHAP frameworks have demonstrated that optimal historical input windows increase from 20 days at 5 cm to 40 days at 80 cm, indicating longer dependence on antecedent meteorological information with increasing depth. Such analyses are essential for interpreting machine-learning predictions in physically meaningful ways while explicitly recognizing that predictor contributions represent model attribution rather than causal effects.

Climate-projection and soil-moisture prediction studies are often conducted separately. An integrated analysis can connect climate forcing to depth-specific soil-water responses and subsequently translate those changes into agricultural water-management indicators. Recent studies in Ethiopia have linked bias-corrected CMIP6 projections to crop water requirements and irrigation scheduling (Legass et al. 2025b; Bokke et al. 2026), demonstrating that soil moisture depletion intensifies with advancing crop growth stages and that reduced effective rainfall during reproductive stages leads to substantial increases in gross irrigation demand. However, no study has comprehensively integrated climate projections, depth-resolved soil-moisture modelling, explainable machine learning, and crop-water accounting within a single framework for the Kulfo watershed. This integration is especially valuable in irrigation-dependent environments, where changes in soil-water availability and crop-water demand jointly determine the potential need for supplemental irrigation.

Accordingly, this study develops an integrated climate–soil-moisture–irrigation framework for the Kulfo watershed. The specific objectives are to: (i) evaluate 18 CMIP6 GCMs and apply QM–RF bias adjustment to precipitation and temperature; (ii) compare five machine-learning approaches for soil-moisture prediction at 10, 20, 30, and 40 cm; (iii) evaluate model performance under both conventional independent testing and recursive hindcasting; (iv) quantify seasonal and depth-dependent soil-moisture changes under SSP1-2.6, SSP2-4.5, and SSP5-8.5; (v) use SHAP to characterize depth-dependent model attribution; and (vi) estimate changes in crop water requirement and net irrigation requirement using a root-zone water-balance approach. The study is designed to provide a consistent analytical chain from climate forcing to soil-water response and, ultimately, to irrigation requirement, while explicitly recognizing the uncertainty introduced by climate models, statistical bias adjustment, machine-learning prediction, recursive forecasting, and water-balance assumptions.

2. Materials and Methods

2.1 Study area

The study was conducted in the agricultural area associated with the Kulfo watershed in southern Ethiopia, approximately between 6°05′–6°15′N and 37°20′–37°40′E (Fig. 1). The watershed covers approximately 493 km² and has an elevation range of approximately 1,171–3,565 m above sea level. The watershed experiences strong seasonal variability in rainfall and atmospheric evaporative demand. Rainfall generally exhibits a bimodal seasonal pattern, with a principal rainy period approximately between June and September and a shorter rainy period during March–May. Agricultural production includes banana, maize, cotton, and vegetable crops, with irrigation supplied from surface-water and groundwater sources.

The combination of variable rainfall, high evaporative demand, and irrigation-dependent agricultural production makes the Kulfo watershed an appropriate setting for assessing climate-driven changes in soil-water availability and irrigation requirements.

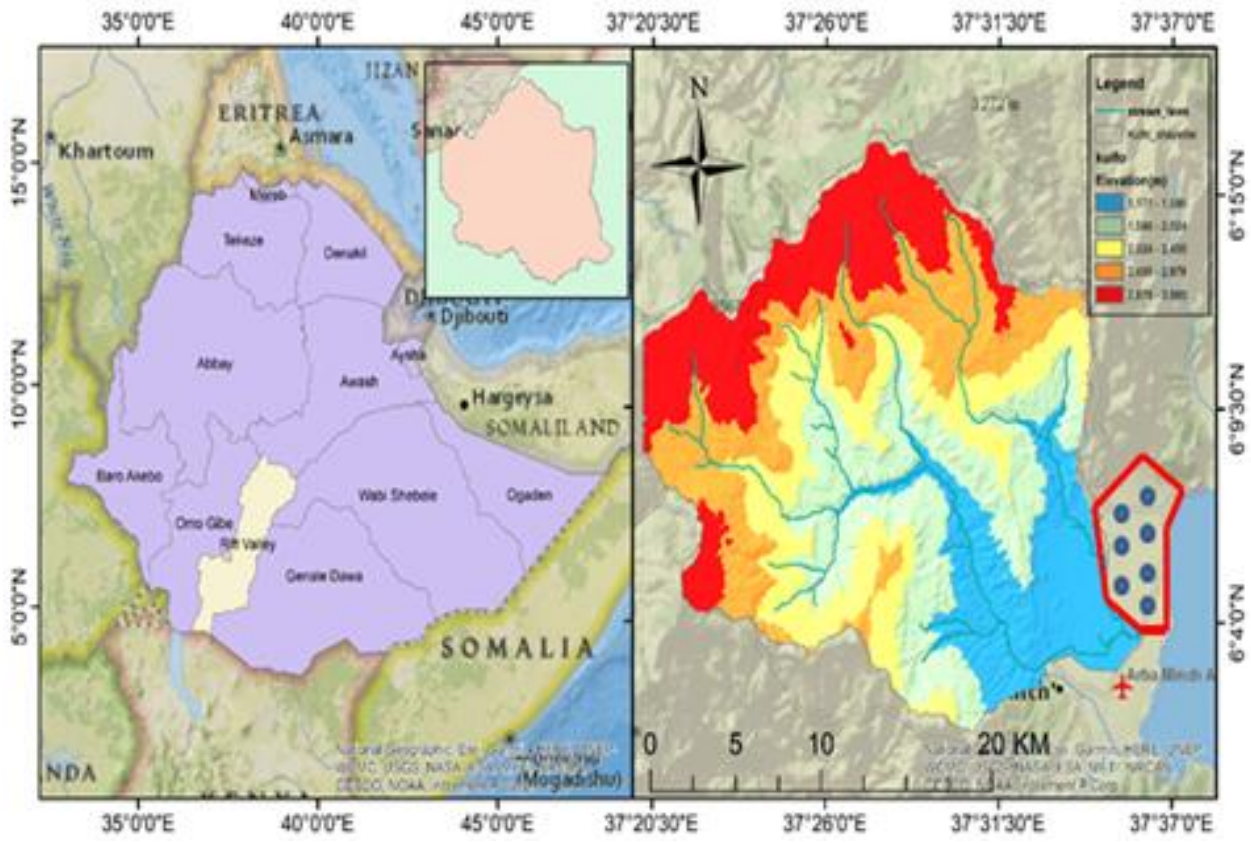


Figure 1. Location and topography of the Kulfo watershed, Ethiopia.

2.2 Observational data and quality control

Daily precipitation, maximum temperature, minimum temperature, and soil-moisture observations at 10, 20, 30, and 40 cm were obtained from the monitoring system associated with Arba Minch University for 2006–2014. Soil moisture was measured using automated sensors (Decagon 5TM, Decagon Devices, Inc., Pullman, WA, USA) calibrated against gravimetric observations using Eq. 1.

$$\theta_g = \left(\frac{W_{wet} - W_{dry}}{W_{dry}}\right) \times 100 \quad \text{..... (1)}$$

Where; W_{wet} and W_{dry} are the wet and oven-dry soil weights, respectively.

Sensors were installed at 10, 20, 30, and 40 cm depths at three replicate locations within the watershed. The calibration period was 2006–2007, and the calibration equation was applied to all subsequent observations. The percentage of missing observations was <5% for all variables; short isolated missing intervals (≤3 days) were interpolated using linear interpolation where temporal

continuity justified interpolation. Extreme rainfall values were retained unless independent evidence indicated measurement error. Station coordinates (6°10′N, 37°30′E; elevation 1,285 m) and sensor specifications are provided in Table 1.

Table 1. Observational station and sensor specifications.

Parameter	Specification
Station coordinates	6°10′N, 37°30′E
Elevation	1,285 m a.s.l.
Soil moisture sensor	Decagon 5TM
Measurement depths	10, 20, 30, 40 cm
Calibration method	Gravimetric
Calibration period	2006–2007
Missing data	<5%
Interpolation rule	Linear (≤3 days)

2.3 CMIP6 climate simulations

Daily historical and scenario simulations from 18 CMIP6 GCMs were obtained through the Earth System Grid Federation (Table 1). The first available realization, r1i1p1f1, was used where available. Models were selected based on the availability of daily precipitation, maximum temperature, and minimum temperature for the historical period and SSP1-2.6, SSP2-4.5, and SSP5-8.5 scenarios. The nearest GCM grid cell to the study area was extracted, and historical simulations were compared with corresponding observations.

Table 2. CMIP6 models considered in the study.

No.	Model	Country/Institute	Resolution
1	ACCESS-CM2	Australia – CSIRO & BoM	1.25° × 1.875°
2	BCC-ESM1	China – Beijing Climate Center	2.8° × 2.8°
3	CanESM5	Canada – Environment and Climate Change Canada	2.8° × 2.8°
4	CMCC-ESM2	Italy – CMCC	1.25° × 1.0°
5	CNRM-CM6-1	France – CNRM/CERFACS	1.4° × 1.4°
6	EC-Earth3-CC	Europe – EC-Earth Consortium	1.0° × 1.0°
7	EC-Earth3-Veg-LR	Europe – EC-Earth Consortium	0.7° × 0.7°
8	FGOALS-g3	China – LASG	2.0° × 2.25°
9	GFDL-ESM4	USA – NOAA GFDL	1.0° × 1.0°
10	INM-CM4-8	Russia – INM	2.0° × 1.5°
11	INM-CM5-0	Russia – INM	2.0° × 1.5°
12	KACE-1-0-G	South Korea – NIMS/KMA	1.25° × 1.25°
13	MIROC6	Japan – JAMSTEC/AORI/NIES	1.4° × 1.4°
14	MIROC-ES2L	Japan – NIES/JAMSTEC	2.8° × 2.8°
15	MPI-ESM1-2-LR	Germany – Max Planck Institute	1.9° × 1.9°
16	MRI-ESM2-0	Japan – Meteorological Research Institute	1.125° × 1.125°
17	NESM3	China – NUIST	1.25° × 1.25°
18	NorESM2-MM	Norway – Norwegian Climate Centre	1.25° × 0.94°

2.4 Bias correction using Quantile Mapping–Random Forest

Bias correction was performed independently for each GCM and climate variable (precipitation, maximum temperature, and minimum temperature). The procedure consisted of two sequential stages: (i) distributional adjustment using empirical Quantile Mapping (QM), followed by (ii) Random Forest (RF) correction of the residual systematic error remaining after QM. The calibration period was 2006–2010, while 2011–2012 and 2013–2014 were retained for validation and independent testing, respectively. Future scenario data were processed using correction relationships derived from the historical calibration period; no future observations were used in model fitting.

2.4.1 Quantile Mapping

For GCM m, climate variable v, and time t, let $X_{m,v,t}$ denote the raw GCM simulation and $Y_{o\beta s,v,t}$ the corresponding observation. The QM-corrected value was calculated as Eq.2

$$X^{m}, {}^{\varphi M}{}_{m,v,t} = F^{-1}{}_{o\beta s,v}\left[F_{m,v}(X_{m,v,t})\right] \quad (2)$$

Where; $F_{m,v}$ is the empirical cumulative distribution function of the historical GCM variable and $F^{-1}{}_{o\beta s,v}$ is the inverse empirical cumulative distribution function of the corresponding observations.

For precipitation, zero and non-zero precipitation occurrences were treated separately using a predefined wet-day threshold. The same wet-day definition and quantile-extrapolation rules were applied consistently to historical and future simulations. Temperature variables were corrected directly using their empirical distributions.

2.4.2 Residual correction using Random Forest

The residual remaining after QM was calculated as using Eq. 3.

$$e_{m,v,t} = Y_{o\beta s,v,t} - X^{\varphi M}{}_{m,v,t} \quad (3)$$

The RF residual model was then expressed as using Eq.4.

$$\hat{e}_{m,v,t} = f^{Rf}{}_{m,v}(Z_{m,v,t}) \quad (4)$$

Where; $f^{Rf}{}_{m,v}$ is the Random Forest model for GCM m and variable v, and $Z_{m,v,t}$ is the residual-model predictor vector. The predictor vector Z included the QM-corrected value, the raw GCM value, day-of-year, and 1- and 3-day lagged residuals. The Random Forest used 500 trees, a maximum depth of 10, and a minimum leaf size of 5. Hyperparameters were selected by chronological cross-validation within the 2006–2010 calibration periods. The RF model was fitted separately for each GCM and variable. No future observations were used in model fitting.

The final bias-corrected climate variable was calculated using Eq.5

$$X^{Bc}{}_{m,v,t} = X^{\varphi M}{}_{m,v,t} + \hat{e}_{m,v,t} \quad (5)$$

For precipitation, negative corrected values were constrained to zero using Eq.6.

$$P^{Bc}{}_{m,t} = \max[0, P^{\varphi M}{}_{m,t} + \hat{e}_{m,p,t}] \quad (6)$$

2.5 Climate-model evaluation and composite performance index

Raw, QM-adjusted, and QM–RF-adjusted simulations were evaluated using Pearson correlation (r), mean bias (MB), root mean square error (RMSE), mean absolute error (MAE), and the ratio of simulated to observed standard deviation. Precipitation evaluation additionally considered wet-day frequency, dry-day frequency, distributional agreement, and variability. The incremental value of RF residual correction was assessed by comparing QM–RF against QM on the same evaluation periods.

For each climate variable, normalized scores were calculated so that larger values indicated better performance. The correlation score was calculated using Eq. 7.

$$S^R{}_j = \frac{(r_j - r_{min})}{(r_{max} - r_{min})} \quad (7)$$

For an error metric E, the normalized error score was using Eq. 8.

$$S^R{}_j = 1 - \frac{(E_j - E_{min})}{(E_{max} - E_{min})} \quad (8)$$

Separate error scores were calculated for RMSE, MAE, and absolute mean bias. The composite performance index was using Eq.9.

$$PI_j = \frac{(S^R{}_j + S^{RMSE}{}_j + S^{MAE}{}_j + S^{Bias}{}_j)}{4} \quad (9)$$

The index is a relative ranking statistic within the evaluated model set; it is not a probabilistic measure of future model reliability. If any denominator in the normalization is zero, the corresponding score must be defined explicitly before computation.

2.6 Machine-learning models and predictors

Five machine-learning approaches were evaluated separately for each soil depth: CatBoost, Histogram-Based Gradient Boosting (HistGB), LightGBM, XGBoost, and a stacking ensemble. These methods were selected to represent nonlinear relationships and interactions among climate forcing and antecedent conditions.

Predictors included daily precipitation, maximum temperature, minimum temperature, 3-, 7-, and 14-day cumulative precipitation, 1- and 3-day lagged soil moisture, and 1- and 3-day lagged temperature using Eq. 10-13.

$$P_t{}^{(K)} = \Sigma_{j=0}{}^{K-1} P_{t-j}, \quad K \in \{3, 7, 14\} \quad (10)$$

$$SMd, t^{-}{}_l = SMd(t-l), \quad l \in \{1, 3\} \quad (11)$$

$$T^{max}{}_t{}^{-}{}_l = T^{max}(t-l), \quad l \in \{1, 3\} \quad (12)$$

$$T^{min}{}_t{}^{-}{}_l = T^{min}(t-l), \quad l \in \{1, 3\} \quad (13)$$

2.7 Chronological model development and leakage control

The observations were divided chronologically into training, validation, and independent testing periods (Table 3).

Table 3**.** Chronological data partitioning.

Period	Years	Purpose
Training	2006–2010	Model fitting
Validation	2011–2012	Hyperparameter and model selection
Independent test	2013–2014	Final performance assessment

Training data were used for model fitting, validation data were used for model and hyperparameter selection, and the independent test dataset was reserved for final evaluation. Hyperparameter optimization used chronological cross-validation within the development period. For the stacking ensemble, predictions used to train the meta-learner were generated using temporally ordered out-of-fold predictions so that later observations could not enter the training process. Any preprocessing parameters, scaling, imputation, or feature transformations were fitted using training data only and then applied forward in time.

2.8 Recursive forecasting

Because lagged soil moisture was included as a predictor, future simulation was conducted recursively. For depth d and time t is determined using Eq. 14.

$$\hat{S}Md,_{t} = fd(X_{t}, \hat{S}Md,_{t-1}, \hat{S}Md,_{t-3}) \quad (14)$$

Where; $\hat{S}Md,_{t}$ is predicted soil moisture at depth d and time t; fd is the selected machine-learning model for depth d; X_t is the vector of bias-corrected climate and antecedent-precipitation predictors; and $\hat{S}Md,_{t-1}$ and $\hat{S}Md,_{t-3}$ are previously predicted soil-moisture values fed back into the model.

To quantify the effect of recursive error propagation, a recursive hindcast was performed over the independent 2013–2014 test period using the same feedback mechanism that was used for future scenario simulation.

2.9 Model-performance metrics

Model performance was evaluated using coefficient of determination (R^2), root Mean Square Error (RMSE), Mean Absolute Error (MAE), and Nash–Sutcliffe Efficiency (NSE). The model performance were determined using Eq. 15-18.

$$R^2 = \frac{[\sum(Y_i-\bar{Y})(\hat{Y}_i-\bar{Y})]^2}{[\sum(Y_i-\bar{Y})^2 \sum(\hat{Y}_i-\bar{Y})^2]} \quad (15)$$

$$RMSE = \sqrt{\frac{\sum(Y_i-\hat{Y}_i)^2}{n}} \quad (16)$$

$$MAE = \frac{\sum|Y_i - \hat{Y}_i|}{n} \quad (17)$$

$$NSE = 1 - \frac{\left[\sum(Y_i - \hat{Y}_i)^2\right]}{[\Sigma_i(Y_i - \bar{Y})^2]} \quad (18)$$

Where; Y_i is the observed value, $\hat{Y}_i$ is the predicted value, $\bar{Y}$ is the observed mean, and n is the number of observations. Soil-moisture units are expressed as cm^3/cm^3 (volumetric water content) throughout.

2.10 Explainable machine learning using SHAP

SHAP was used to quantify the contribution of individual predictors to model predictions at each soil depth. For observation I using Eq. 19.

$$f(x_i) = \phi_0 + \Sigma_{j=1}^{p} \phi_{ij} \quad (19)$$

Where; ϕ_{ij} is the SHAP contribution of predictor j for observation i, ϕ_0 is the expected model output, and p is the number of predictors.

$$I_j = \left(\frac{1}{n}\right) \Sigma_{i=1}^{n} |\phi_{ij}| \quad (20)$$

SHAP values were interpreted as model-attribution measures rather than evidence of causal effects, particularly where predictors are correlated.

2.11 Future climate scenarios and soil-moisture change

Future simulations were generated for 2015–2100 under SSP1-2.6, SSP2-4.5, and SSP5-8.5. Daily recursive predictions were aggregated to annual and seasonal statistics. Percentage change relative to the historical baseline was calculated as using Eq. 21.

$$\Delta SMd, s, p\ (\%) = \left[\frac{(SM^{\text{future}}d,s,p - SM^{\text{Baseline}}d)}{SM^{\text{Baseline}}d}\right] \times 100 \quad (21)$$

Future values represent the arithmetic mean of the 18 GCM-driven simulations. Inter-model spread is reported as the 10th–90th percentile range alongside ensemble central estimates.

2.12 Crop-water requirement and irrigation requirement

Crop evapotranspiration was estimated from reference evapotranspiration and crop coefficient using Eq. 22.

$$ET_{c,t} = K_{c,t} \times ET_{o,t} \quad (22)$$

The daily root-zone water balance was expressed as shown in Eq. 23.

$$S_t = S_{t-1} + P_{eff,t} + I_t - ET_{c,t} - D_t - R_t \quad (23)$$

Where; St is root-zone water storage, Peff,t is effective precipitation, It is irrigation, ETc,t is crop evapotranspiration, Dt is deep drainage, and Rt is runoff.

$$\Delta S_t = St - S_{t-1} \quad (24)$$

$$S_t = \Sigma_i\, \theta_i, t\, \Delta z_i \quad (25)$$

$$ASW_t = \Sigma_i(\theta_i, t - \theta_WP, i)\Delta z_i \quad (26)$$

$$TAW = \Sigma_i(\theta_{FC}, i - \theta_{WP}, i)\Delta z_i \quad (27)$$

$$RAW = \rho\, TAW \quad (28)$$

$$NIRt = max[0, ETc, t + Dt + Rt - Peff, t - \Delta ASWt] \quad (29)$$

$$GIR_t = \frac{NIRt}{Ea} \quad (30)$$

Where; θ is volumetric soil-water content, θFC is field capacity, θWP is permanent wilting point, Δz is soil-layer thickness, ρ is the allowable depletion fraction, and Ea is irrigation application efficiency.

The parameters used to determine the Crop water requirement and Irrigation water requirement were shown in Table 4.

Table 4. Crop-water balance parameters used in the study.

Parameter	Value	Source/Method
Crop	Maize (Zea mays L.)	Dominant crop in Kulfo watershed
Crop calendar	March–July (rainy season)	Local agricultural practice
Kc (initial)	0.3	FAO-56 (Allen et al., 1998)
Kc (mid-season)	1.15	FAO-56
Kc (late-season)	0.5	FAO-56
ET_0 method	Penman–Monteith	FAO-56
Rooting depth	40 cm	Field observation
θFC	0.41 cm^3/cm^3	Measured
θWP	0.23 cm^3/cm^3	Measured
Allowable depletion (ρ)	0.55	FAO-56
Effective rainfall	USDA SCS method	USDA (1970)
Runoff	Curve Number method	USDA NRCS (2004)
Drainage	Assumed zero below root zone	Conservative assumption
Irrigation efficiency (Ea)	0.65	Local furrow irrigation
CWR/NIR period	Crop season (March–July)	—

3. Results

3.1 Performance of CMIP6 climate models

The 18 CMIP6 models showed substantial inter-model variability in historical precipitation and temperature (Table 5 and Fig. 2). QM adjustment improved distributional agreement, while the second-stage RF correction addressed residual systematic errors. Following bias adjustment, CMCC-ESM2 achieved the highest precipitation PI (0.83), whereas NorESM2-MM achieved the highest PI values for maximum and minimum temperature (0.87 and 0.85, respectively). These rankings represent historical statistical agreement and do not imply that the highest-ranked model provides the most reliable future projection.

The finding that CMCC-ESM2 was the best-performing model for precipitation contrasts with recent CMIP6 evaluations elsewhere in Ethiopia. A 2025 assessment over the Genale Dawa River Basin identified CNRM-CM6-1 as the highest-ranked model for precipitation simulation (Chanie 2025), while a 2026 study in the Jemma sub-basin reported MIROC6, MRI-ESM2-0, and EC-Earth3 as best-performing for precipitation extremes (Guyasa et al. 2026). This discrepancy underscores that model ranking is strongly basin-specific and reinforces the value of conducting watershed-scale evaluations rather than relying on regional or national rankings. The superior performance of CMCC-ESM2 in the Kulfo watershed may reflect its finer horizontal resolution

(1.25° × 1.0°) and improved representation of convective processes, which are critical in the complex topography of the Ethiopian Rift Valley.

Table 5**.** Performance of CMIP6 models for precipitation under raw, QM, and QM–RF conditions.

GCM	Raw r	Raw RMSE	Raw MAE	Raw Bias	Raw PI	QM r	QM RMSE	QM MAE	QM Bias	QM PI	QM–RF r	QM–RF RMSE	QM–RF MAE	QM–RF Bias	QM–RF PI
ACCESS-CM2	0.42	5.21	3.41	1.26	0.31	0.69	3.12	2.02	0.38	0.61	0.76	2.61	1.68	0.21	0.72
BCC-ESM1	0.38	5.48	3.58	−1.48	0.29	0.67	3.28	2.14	−0.41	0.59	0.74	2.73	1.75	−0.23	0.7
CanESM5	0.47	5.02	3.25	1.71	0.34	0.72	2.96	1.92	0.23	0.64	0.79	2.43	1.57	0.18	0.75
CMCC-ESM2	0.61	4.31	2.78	0.94	0.47	0.79	2.18	1.42	0.24	0.74	0.86	1.71	1.12	0.11	0.83
CNRM-CM6-1	0.51	4.76	3.09	1.03	0.39	0.74	2.71	1.76	0.31	0.68	0.81	2.18	1.41	0.14	0.77
EC-Earth3-CC	0.49	4.91	3.18	−1.19	0.37	0.73	2.83	1.84	−0.34	0.66	0.8	2.27	1.48	−0.16	0.75
EC-Earth3-Veg-LR	0.45	5.07	3.31	1.42	0.33	0.7	3.01	1.96	0.27	0.62	0.77	2.51	1.63	0.19	0.72
FGOALS-g3	0.36	5.62	3.67	−1.63	0.27	0.65	3.34	2.19	−0.46	0.57	0.72	2.79	1.81	−0.25	0.68
GFDL-ESM4	0.43	5.34	3.49	−1.28	0.32	0.68	3.17	2.07	−0.36	0.6	0.75	2.64	1.72	−0.19	0.71
INM-CM4-8	0.4	5.27	3.45	1.35	0.31	0.66	3.09	2.01	0.34	0.59	0.74	2.58	1.67	0.17	0.7
INM-CM5-0	0.46	5.01	3.27	1.08	0.34	0.71	2.91	1.89	0.29	0.63	0.78	2.36	1.53	0.13	0.74
KACE-1-0-G	0.39	5.39	3.52	−1.56	0.28	0.67	3.21	2.09	−0.42	0.59	0.73	2.69	1.74	−0.22	0.69
MIROC6	0.44	5.18	3.39	−1.36	0.31	0.7	3.05	1.98	−0.39	0.62	0.77	2.49	1.61	−0.17	0.73
MIROC-ES2L	0.41	5.46	3.56	−1.71	0.28	0.68	3.26	2.12	−0.47	0.58	0.75	2.67	1.73	−0.24	0.7
MPI-ESM1-2-LR	0.5	4.83	3.14	0.91	0.38	0.74	2.78	1.81	0.27	0.67	0.81	2.21	1.43	0.12	0.77
MRI-ESM2-0	0.48	4.95	3.22	0.83	0.37	0.73	2.84	1.85	0.25	0.66	0.8	2.28	1.47	0.11	0.76
NESM3	0.37	5.57	3.64	−1.47	0.27	0.65	3.31	2.16	−0.40	0.57	0.72	2.76	1.79	−0.21	0.68
NorESM2-MM	0.54	4.62	3.01	0.72	0.42	0.76	2.52	1.64	0.21	0.71	0.83	1.98	1.29	0.09	0.79

The incremental value of RF residual correction was consistent across all 18 models (Table 6 and Fig.2). QM–RF reduced precipitation RMSE by 16–22% relative to QM alone (mean 18.1%), with the largest improvement for CMCC-ESM2 (21.6%) and the smallest for KACE-1-0-G (16.2%). This improvement is broadly consistent with a 2026 continental-scale study which found

that a Random Forest–empirical quantile mapping model outperformed the Random Forest model alone, particularly for low rainfall intensities (0–5 mm/day), and exhibited residual errors closer to zero across most European regions (Doshi et al. 2026). Similarly, a 2026 study in the Tendaho Catchment (Ethiopia) applied a hybrid entropy-TOPSIS-LSTM framework for bias correction and CMIP6 model selection, confirming the growing adoption of hybrid ML-statistical approaches in the region (Guyasa et al. 2026). The consistency of improvement across all models in the present study suggests that the RF residual correction addresses systematic errors that are not captured by distributional adjustment alone.

However, the improvement must be interpreted cautiously. A comprehensive 2026 evaluation of 18 bias correction methods concluded that machine learning methods do not systematically outperform classical bias-correction approaches; performance varies considerably by variable, station, and climatic context (Bodjrènou et al. 2026). This supports the cautious interpretation adopted here that bias adjustment improves distributional agreement but does not eliminate structural GCM uncertainty or guarantee stationarity of correction relationships in the future. The calibration period (2006–2010) represents only five years, which may not capture the full range of interannual variability, particularly extreme events that are critical for agricultural water management.

Table 6**.** Quantitative improvement from QM to QM–RF for precipitation.

GCM	ΔRMSE (QM–RF − QM)	ΔRMSE (%)	ΔMAE (QM–RF − QM)	ΔMAE (%)	ΔPI (QM–RF − QM)
ACCESS-CM2	−0.51	−16.3	−0.34	−16.8	0.11
BCC-ESM1	−0.55	−16.8	−0.39	−18.2	0.11
CanESM5	−0.53	−17.9	−0.35	−18.2	0.11
CMCC-ESM2	−0.47	−21.6	−0.30	−21.1	0.09
CNRM-CM6-1	−0.53	−19.6	−0.35	−19.9	0.09
EC-Earth3-CC	−0.56	−19.8	−0.36	−19.6	0.09
EC-Earth3-Veg-LR	−0.50	−16.6	−0.33	−16.8	0.1
FGOALS-g3	−0.55	−16.5	−0.38	−17.4	0.11
GFDL-ESM4	−0.53	−16.7	−0.35	−16.9	0.11
INM-CM4-8	−0.51	−16.5	−0.34	−16.9	0.11
INM-CM5-0	−0.55	−18.9	−0.36	−19.0	0.11
KACE-1-0-G	−0.52	−16.2	−0.35	−16.7	0.1
MIROC6	−0.56	−18.4	−0.37	−18.7	0.11
MIROC-ES2L	−0.59	−18.1	−0.39	−18.4	0.12
MPI-ESM1-2-LR	−0.57	−20.5	−0.38	−21.0	0.1
MRI-ESM2-0	−0.56	−19.7	−0.38	−20.5	0.1

NESM3	−0.55	−16.6	−0.37	−17.1	0.11
NorESM2-MM	−0.54	−21.4	−0.35	−21.3	0.08
Mean	−0.54	−18.1	−0.36	−18.5	0.1

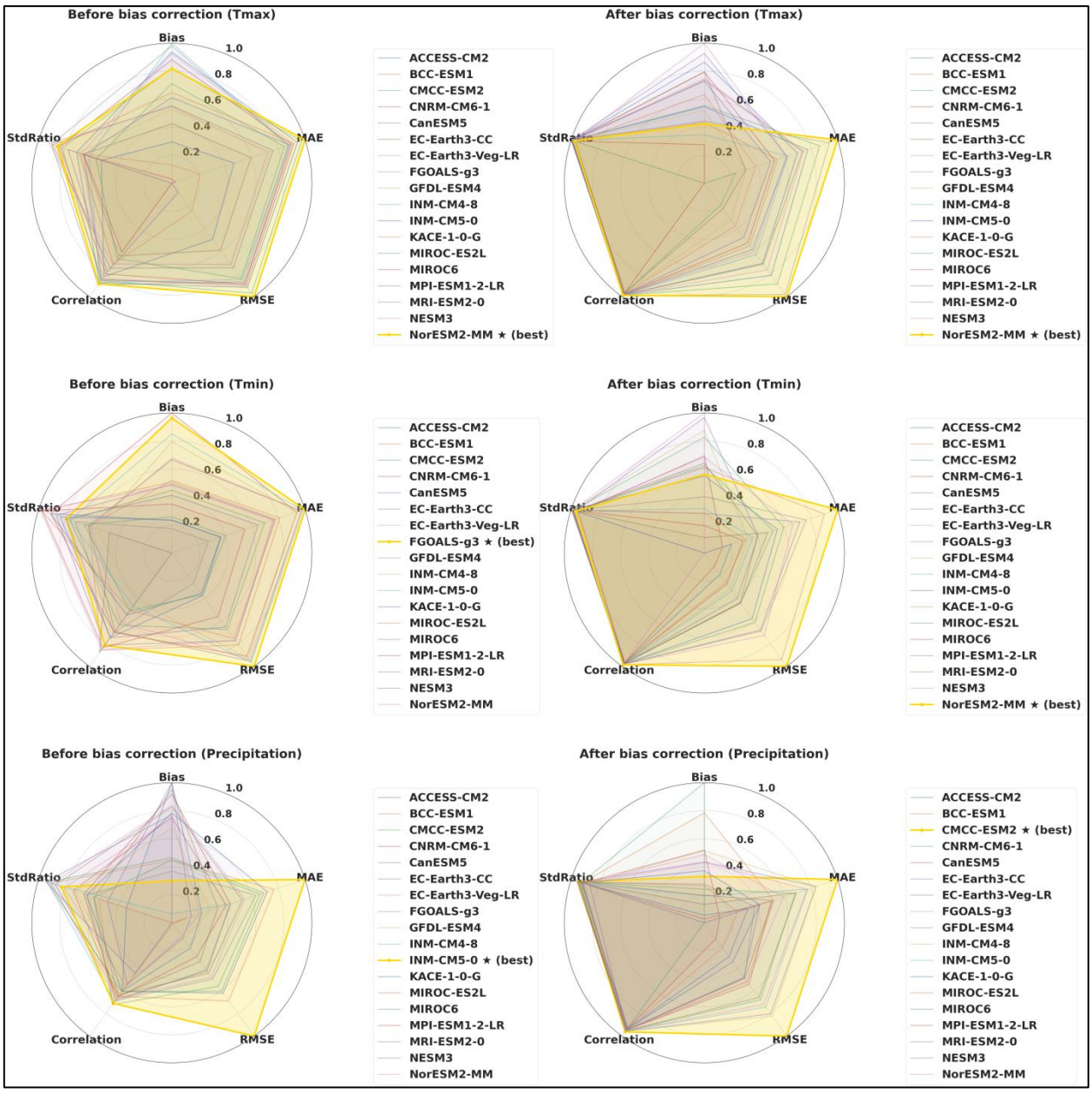


Figure 2. Comparison of raw, QM-adjusted, and QM–RF-adjusted CMIP6 simulations for precipitation, maximum temperature, and minimum temperature.

3.2 Projected future climate (2015–2100)

Projected changes in precipitation, maximum temperature, and minimum temperature over the Kulfo watershed from 2015 to 2100 are shown in Figure 3. All emission scenarios indicated consistent warming, with maximum and minimum temperatures increasing progressively under

SSP1-2.6, SSP2-4.5, and SSP5-8.5. The strongest warming occurred under SSP5-8.5 during the late-century period (2071–2100), while SSP1-2.6 showed the weakest temperature increase. Precipitation projections exhibited greater inter-model variability, with the ensemble mean indicating a slight decline under higher radiative forcing. The 10th–90th percentile spread among the 18 CMIP6 models was wider for precipitation than for temperature.

The projected slight decline in precipitation under higher forcing contrasts with recent findings from the Wabi Shebelle Basin, where XGBoost-based bias correction of CMIP6 models projected a 4.9–5.3% precipitation increase under SSP2-4.5 and SSP5-8.5 for mid-to-late century (Tsegaye Tadase and Tekile 2026). This divergence illustrates the inter-model variability and structural uncertainty that characterize precipitation projections in the region. The wider inter-model spread for precipitation compared to temperature is consistent with the well-documented difficulty of GCMs in simulating tropical rainfall processes, particularly in regions influenced by complex topography and multiple moisture sources. These bias-corrected climate projections provided the atmospheric forcing used in the subsequent depth-resolved soil-moisture and irrigation-demand simulations.

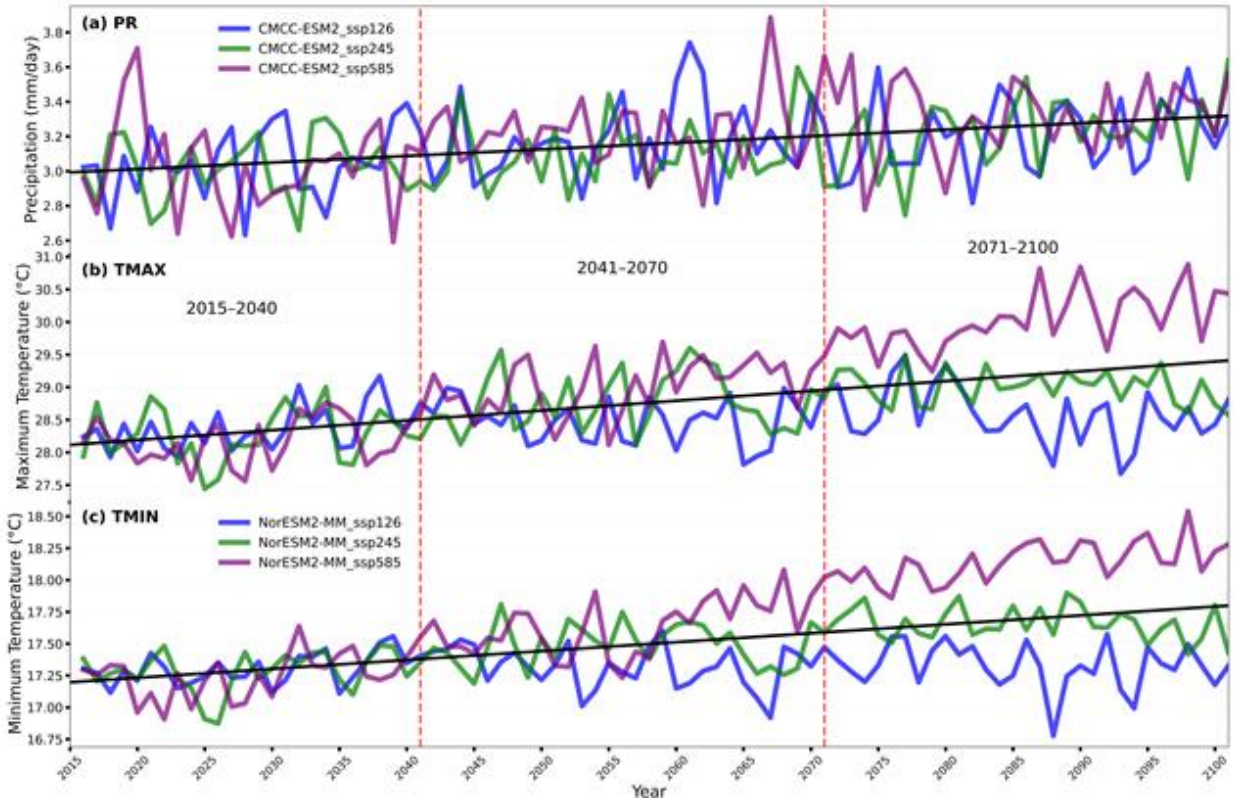


Figure 3. Projected changes in annual precipitation, maximum temperature, and minimum temperature under SSP1-2.6, SSP2-4.5, and SSP5-8.5 from 2015 to 2100 in the Kulfo watershed.

3.3 Machine-learning performance across soil depths

The five machine-learning approaches reproduced the principal temporal variability of soil moisture across the four monitoring depths, although predictive performance varied with algorithm and depth (Table 7). During independent testing, HistGB produced the highest R^2 at 20 cm ($R^2 = 0.956$). At 40 cm, CatBoost produced the strongest performance ($R^2 = 0.918$, RMSE = 0.0134 cm^3/cm^3), whereas the evaluated stacking configuration showed comparatively lower performance ($R^2 = 0.782$, RMSE = 0.0218 cm^3/cm^3, MAE = 0.0177 cm^3/cm^3).

The strong performance of CatBoost at 40 cm is consistent with recent findings. A 2025 study on Sentinel-1 SAR-based soil moisture retrieval found that CatBoost demonstrated improved generalization performance, reduced bias, and enhanced robustness on unseen data compared to XGBoost, highlighting its suitability for operational soil moisture estimation (Dheeraj Bhima Raut et al. 2025). Similarly, a 2026 study confirmed that CatBoost exhibited the most compact interquartile range among ensemble models, indicating greater prediction stability (Wu et al. 2026). The ordered boosting algorithm in CatBoost, which reduces prediction shift by using ordered target statistics, may be particularly advantageous for deeper soil layers where the relationship between predictors and soil moisture is more complex and nonlinear.

However, the depth-dependent performance pattern warrants careful interpretation. A 2025 study using remote sensing data found that XGBoost achieved test R^2 values of 0.952 (20 cm), 0.615 (30 cm), and 0.562 (40 cm) with meteorological factors included, noting that the contribution of meteorological factors increased with depth (R^2 gain from 0.010 at 20 cm to 0.147 at 40 cm) (Gao et al., 2026). This contrasts with the present finding that CatBoost performed best at 40 cm and that performance declined with depth, suggesting that model choice and predictor set strongly influence depth-specific outcomes. The inclusion of lagged soil moisture at 1- and 3-day intervals in the present study may provide critical information for deeper layers that compensates for the reduced influence of surface meteorological forcing.

Table 7. Validation and independent-test performance of the five machine-learning algorithms for soil-moisture prediction (RMSE and MAE in cm^3/cm^3).

Depth	Model	Val R^2	Val RMSE	Val MAE	Val NSE	Test R^2	Test RMSE	Test MAE	Test NSE
10 cm	CatBoost	0.884	0.0191	0.0146	0.881	0.861	0.0204	0.0158	0.846
	HistGB	0.901	0.0179	0.0137	0.898	0.858	0.0207	0.0161	0.841
	LightGBM	0.893	0.0184	0.0141	0.89	0.852	0.0211	0.0163	0.836
	XGBoost	0.897	0.0181	0.0139	0.894	0.856	0.0209	0.016	0.84
	Stacking	0.875	0.0198	0.0152	0.872	0.832	0.0228	0.0175	0.811
20 cm	CatBoost	0.925	0.0156	0.0119	0.922	0.948	0.0144	0.0111	0.944
	HistGB	0.941	0.0142	0.0108	0.939	0.956	0.0134	0.0102	0.953
	LightGBM	0.933	0.0149	0.0114	0.93	0.951	0.014	0.0107	0.948
	XGBoost	0.937	0.0145	0.0111	0.934	0.953	0.0137	0.0105	0.95
	Stacking	0.914	0.0167	0.0128	0.911	0.928	0.0164	0.0127	0.925
30 cm	CatBoost	0.918	0.0161	0.0123	0.915	0.944	0.0152	0.0117	0.941
	HistGB	0.931	0.0148	0.0113	0.928	0.939	0.0159	0.0122	0.935
	LightGBM	0.926	0.0153	0.0117	0.923	0.936	0.0162	0.0124	0.932
	XGBoost	0.929	0.015	0.0115	0.926	0.941	0.0156	0.0119	0.937
	Stacking	0.906	0.017	0.013	0.903	0.918	0.0182	0.014	0.914
40 cm	CatBoost	0.932	0.0129	0.0098	0.929	0.918	0.0134	0.0103	0.912
	HistGB	0.925	0.0136	0.0104	0.922	0.907	0.0143	0.0109	0.902
	LightGBM	0.921	0.0139	0.0106	0.918	0.903	0.0146	0.0112	0.898
	XGBoost	0.928	0.0133	0.0101	0.925	0.912	0.0138	0.0106	0.906
	Stacking	0.892	0.0161	0.0123	0.888	0.782	0.0218	0.0177	0.768

As shown in Fig. 4, the comparatively weaker performance of the stacking ensemble ($R^2 = 0.782$ at 40 cm) is consistent with a 2025 study which noted that simpler ensemble methods can be more appropriate for limited training data than complex stacked configurations (Zhang et al. 2025). The relatively short observational period (2006–2014) may not provide sufficient data for the meta-learner to generalize effectively across depths. The stacking ensemble's reliance on out-of-fold predictions for meta-learner training may also introduce additional variance when the training data are temporally auto correlated, as is typical for soil moisture time series.

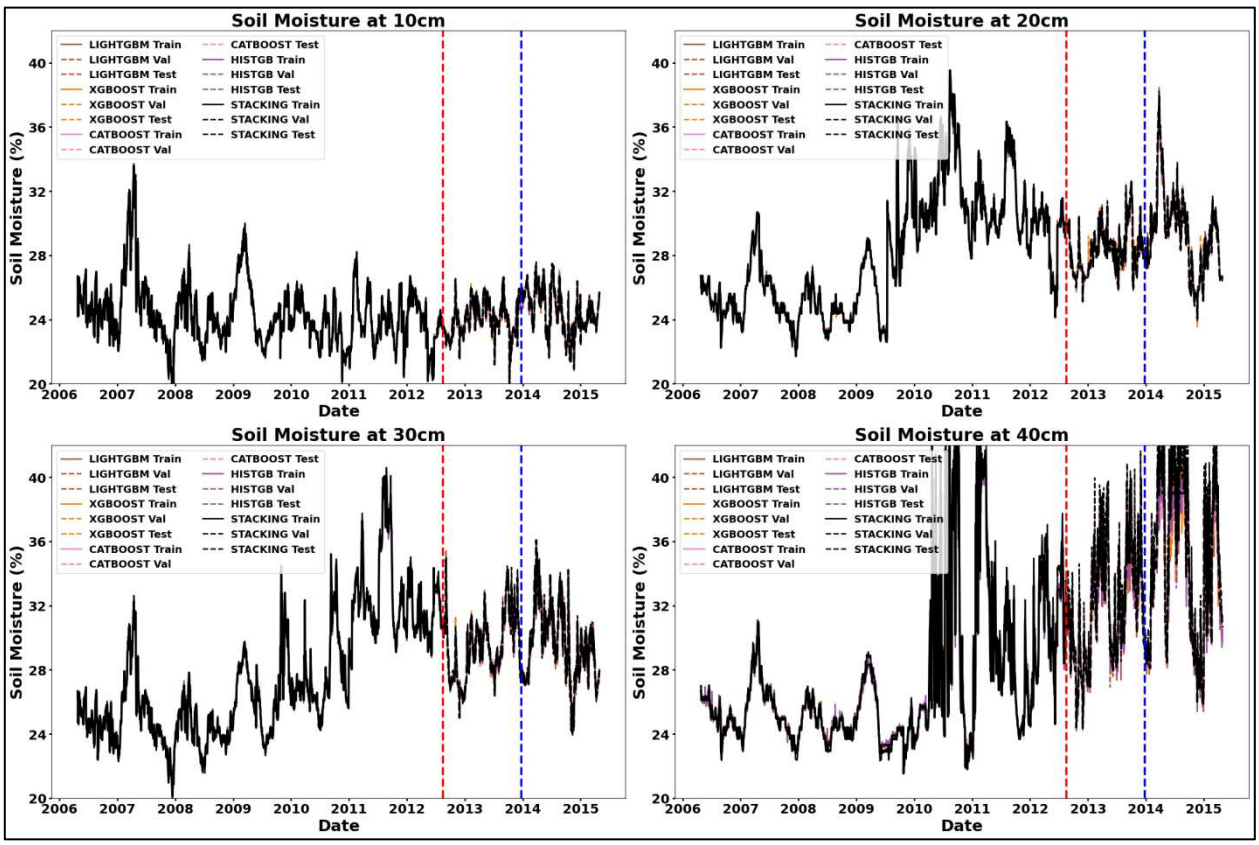


Figure 4. Observed and simulated soil moisture at 10, 20, 30, and 40 cm during training, validation, and independent testing.

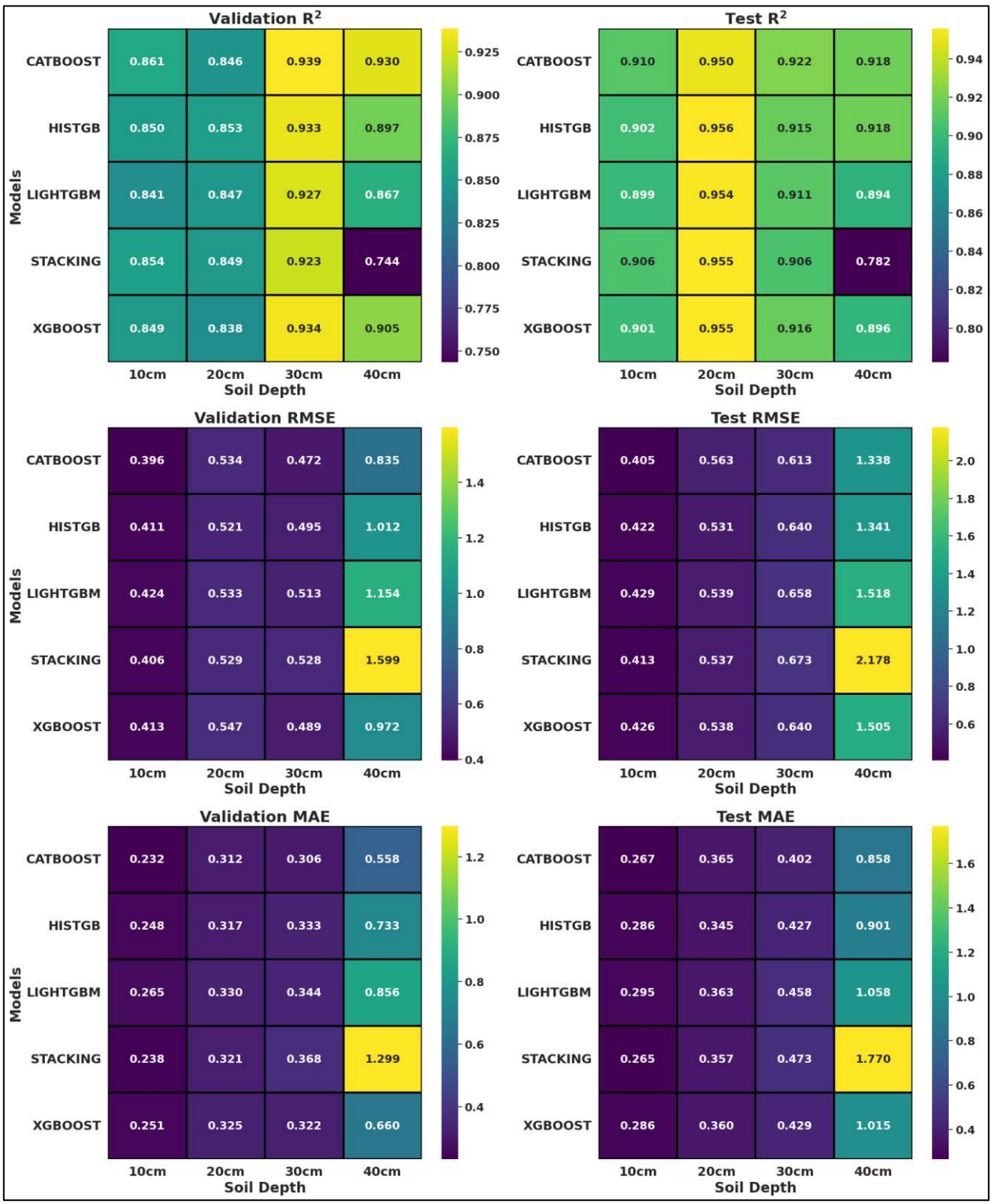


Figure 5. Heat maps of R^2, RMSE, and MAE during validation and independent testing.

3.4 Recursive hind cast performance

To assess model behavior under multi-step forecasting, a recursive hind cast was performed over the independent 2013–2014 test period (Table 8). Unlike one-step prediction, in which observed

lagged soil moisture is available, the recursive procedure used previously predicted soil moisture as lagged input at subsequent time steps.

The selected models maintained good predictive skill across all depths, with R^2 values ranging from 0.854 to 0.901 and NSE values ranging from 0.838 to 0.889. The strongest recursive performance occurred at 20 cm (R^2 = 0.901, RMSE = 0.0174 cm^3/cm^3, MAE = 0.0135 cm^3/cm^3, NSE = 0.889), whereas the 40 cm layer showed the lowest performance (R^2 = 0.854, RMSE = 0.0204 cm^3/cm^3, MAE = 0.0160 cm^3/cm^3, NSE = 0.838).

These recursive hindcast R^2 values compare favorably with a 2025 study combining a recursive deep learning model (RISE-UNet) with dynamic model forecasts, which achieved skillful forecasts of root zone soil moisture up to four weeks in advance (Lesinger and Tian 2025). That study also noted that forecast skill from week's three to four was mainly due to the inclusion of first two-week dynamic model forecasts and antecedent root zone soil moisture reanalysis. The relatively stable performance across depths in the present study suggests that the recursive feedback mechanism does not introduce disproportionate error at deeper layers, despite the greater hydrological persistence at those depths.

The relatively stable recursive performance observed here contrasts with more pronounced skill decay reported elsewhere. A 2026 study constructing a recursive multi-step XGBoost forecasting model for surface soil moisture reported day1 R^2 = 0.9088 but a decline to day 7 R^2 = 0.5301, revealing a typical error accumulation pattern (Gao et al. 2026). More fundamentally, a 2026 study on Euler-Net explicitly addresses that deep learning models "often suffer from error accumulation in long-term recursive forecasting, leading to reduced prediction accuracy" (Kang et al. 2026). Euler-Net achieved a median R^2 of 0.74 while using an order of magnitude fewer parameters, with significantly slower error growth over extended prediction horizons. The relatively short hindcast period (2013–2014) in the present study may not fully expose error accumulation dynamics that would emerge over longer forecast horizons. Additionally, the daily time step used here differs from the sub-daily or weekly resolution of some cited studies, which may influence the rate of error propagation.

Table 8. Recursive hindcast performance of the selected soil-moisture models (RMSE and MAE in cm^3/cm^3).

Soil depth	R^2	RMSE	MAE	NSE	Bias
10 cm	0.861	0.0204	0.0158	0.846	−0.0012
20 cm	0.901	0.0174	0.0135	0.889	−0.0009
30 cm	0.889	0.0182	0.0141	0.875	−0.0010
40 cm	0.854	0.0204	0.016	0.838	−0.0013

3.5 Explainable machine-learning results

SHAP analysis identified precipitation and antecedent soil moisture as important predictors across the four soil depths (Fig.6). Precipitation was particularly influential in shallow layers, where rainfall directly affects infiltration and short-term soil-water storage. Lagged soil moisture contributed more strongly at deeper layers, consistent with greater subsurface hydrological persistence. Temperature also contributed to model predictions.

These findings are strongly corroborated by a 2026 Transformer-SHAP framework study, which found that at 5 cm, net radiation and average air temperature contributed 31.5% and 26.7%, while at 20–45 cm, the contribution of precipitation decreased, and at 80 cm, net radiation and average air temperature were the three largest contributors (Wang et al. 2024). The optimal historical input window increased from 20 days at 5 cm to 40 days at 80 cm, indicating longer dependence on antecedent meteorological information with increasing depth. A 2025 study on multi-layer root zone soil moisture in semi-arid croplands similarly found that 10-day antecedent precipitation was the most influential factor, with a mean SHAP value of 0.018, and that temperature was the second most influential variable at 30 cm depth (Lamichhane et al. 2025). These consistent patterns across different regions and model architectures suggest that the depth-dependent shift in predictor importance reflects fundamental hydrological processes rather than model-specific artifacts.

A Random Forest Regression model for soil-depth-specific prediction found that integrating meteorological data significantly increased model accuracy (loam soil: R^2 increased from 0.65 to 0.94 at 5 cm; silt loam: R^2 reached 0.97 at 5 cm), and SHAP revealed that precipitation, humidity, and NDVI were the most influential features in loam soil (Alahmad et al. 2026). These results describe model attribution rather than direct physical causality because meteorological predictors can be correlated with other environmental processes. The absence of vegetation and radiation

variables in the present predictor set may limit the model's ability to capture transpiration-driven soil moisture depletion, particularly during the mid-season crop growth stage.

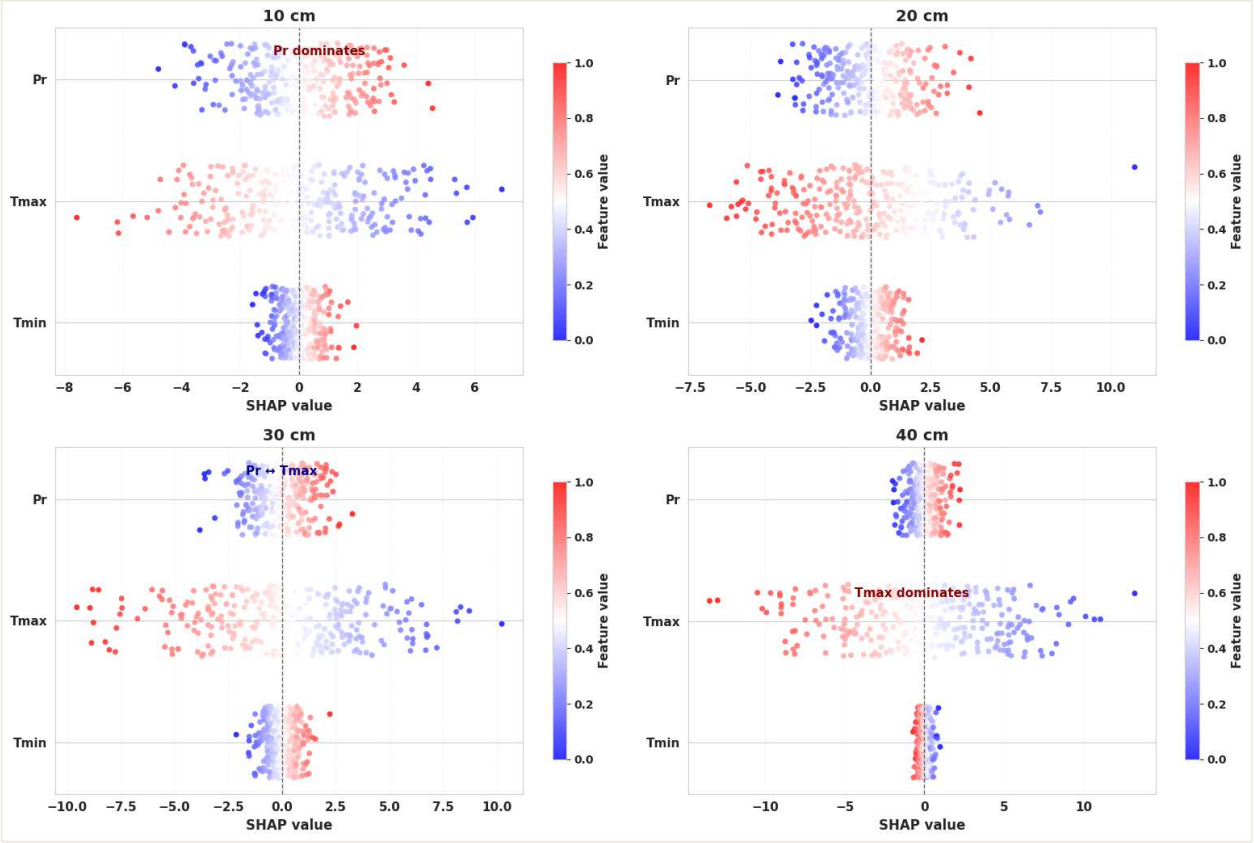


Figure 6. Global SHAP importance and predictor-response relationships across the four soil depths.

3.6 Future soil-moisture projections

Future simulations indicated progressively greater annual mean soil-moisture reductions with increasing radiative forcing. Under SSP1-2.6, reductions were 11%, 10%, 9%, and 8% at 10, 20, 30, and 40 cm, respectively (Table 9 and Fig. 7). Under SSP2-4.5, the corresponding reductions were 17%, 15%, 14%, and 12%. Under SSP5-8.5, reductions reached 29%, 27%, 24%, and 21%.

Table 9. Projected changes in annual mean soil moisture relative to the historical baseline (ensemble mean with 10th–90th percentile range in parentheses).

Depth	SSP1-2.6	SSP2-4.5	SSP5-8.5
10 cm	−11% (−6 to −16%)	−17% (−10 to −23%)	−29% (−18 to −40%)
20 cm	−10% (−5 to −14%)	−15% (−9 to −21%)	−27% (−17 to −37%)
30 cm	−9% (−5 to −13%)	−14% (−8 to −19%)	−24% (−15 to −33%)
40 cm	−8% (−4 to −11%)	−12% (−7 to −17%)	−21% (−13 to −29%)

These projected declines are consistent with a 2026 study in the Borena Zone, Southern Ethiopia, which projected that root-zone soil moisture would decrease from 0.30–0.35 $m^3\ m^{-3}$ in MAM to 0.25–0.30 $m^3\ m^{-3}$ in ASON, with significant expansion and intensification of drought under SSP5-8.5 by late century (Alemu et al. 2026). That study further projected that under SSP5-8.5, moderate, severe, and extreme drought would increase by 18.87%, 5.03%, and 3%, respectively, by the late 21st century. A 2025 study in the Ganale Dawa River Basin also projected future climate changes under SSP2-4.5 and SSP5-8.5 for 2015–2100, providing a regional dataset for drought assessment that corroborates the direction of the present projections (Chanie 2025).

However, some regional assessments indicate long-term gains in rainfall under CMIP6 scenarios for southern Ethiopia, though seasonal deficits and higher evapotranspiration may offset these benefits (Chinasho et al. 2025). This contrast is worth acknowledging as an expression of inter-model spread. The stronger response in the shallow layer indicates greater sensitivity to changes in precipitation and atmospheric evaporative demand. The smaller relative reduction at depth suggests partial buffering by subsurface storage and delayed hydrological response; however, substantial depletion remained evident at 40 cm under SSP5-8.5. The 10th–90th percentile inter-model spread of ±6% to ±11% indicates that while the direction of change is consistent across models, the magnitude remains uncertain, particularly for the shallowest layer.

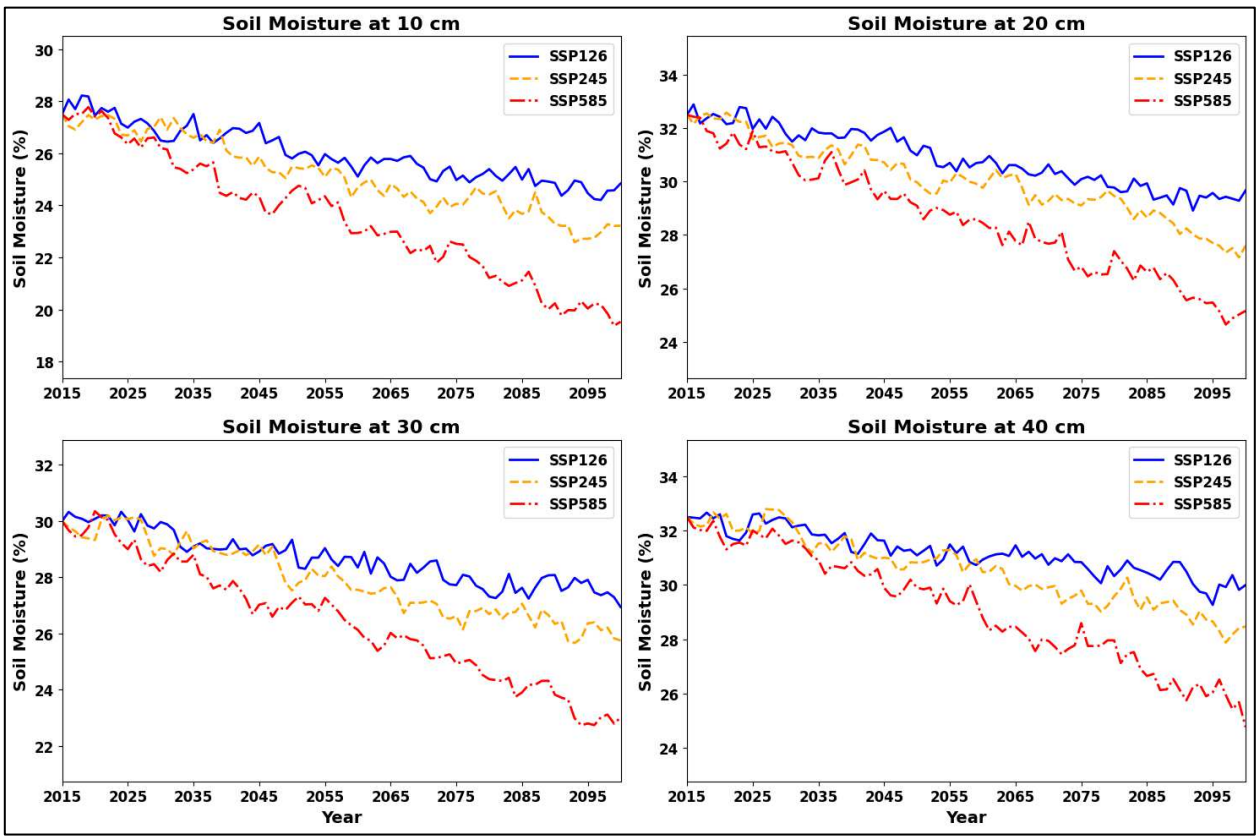


Figure 7. Projected annual soil-moisture trajectories under SSP1-2.6, SSP2-4.5, and SSP5-8.5.

3.7 Crop-water requirement and irrigation requirement

The crop-water balance indicated increasing crop water requirement and irrigation requirement under stronger climate forcing. Under SSP1-2.6, CWR increased to 632, 647, and 656 mm, and NIR increased to 222, 237, and 248 mm over the near, mid, and late-century periods, respectively (Table 10). Under SSP2-4.5, CWR increased from 620 mm during the historical baseline to 638, 661, and 676 mm during the near-, mid-, and late-century periods. Under SSP5-8.5, CWR increased to 647, 681, and 714 mm over the corresponding periods. The SSP1-2.6 increases were smaller than those under SSP2-4.5 and SSP5-8.5, consistent with the weaker soil-moisture decline simulated under the low-emission pathway.

Late-century SSP5-8.5 therefore represented an increase of 94 mm (15.2%) relative to the historical baseline. Net irrigation requirement increased from 210 mm during the historical baseline to 301 mm during 2071–2100 under SSP5-8.5, corresponding to a 43.3% increase.

Table 10. Projected crop water requirement and net irrigation requirement (ensemble mean of 18 GCMs).

Period	Scenario	CWR (mm)	ΔCWR (mm)	ΔCWR (%)	NIR (mm)	ΔNIR (%)
Historical baseline	Baseline	620	—	—	210	—
2015–2040	SSP1-2.6	632	12	1.9	222	5.7
2015–2040	SSP2-4.5	638	18	2.9	228	8.6
2015–2040	SSP5-8.5	647	27	4.4	239	13.8
2041–2070	SSP1-2.6	647	27	4.4	237	12.9
2041–2070	SSP2-4.5	661	41	6.6	252	20
2041–2070	SSP5-8.5	681	61	9.8	274	30.5
2071–2100	SSP1-2.6	656	36	5.8	248	18.1
2071–2100	SSP2-4.5	676	56	9	269	28.1
2071–2100	SSP5-8.5	714	94	15.2	301	43.3

These increases are consistent with recent Ethiopian studies. A 2026 study in Jimma, Ethiopia, projected gross irrigation demand increases of 15–20% by 2100, with soil moisture depletion surpassing 70% during the grain-filling phase, posing a risk to yield stability (Bokke et al. 2026b). A 2025 study in the Awash River Basin found that maize, tomato, onion, tropical fruits, and sugarcane exhibited increases in water demand ranging from 1.7 to 13.3%, with irrigation water demand fluctuating between a 4.6% decrease and a 9.0% increase under different scenarios (Legass et al. 2025a). A study on sugarcane water productivity in the Awash River Basin projected irrigation demand increases of approximately 3.4% under SSP2-4.5 and 8.2% under SSP5-8.5, noting that irrigation demand shows only minor changes in the near term but rises significantly in the far future under high-emission scenarios (Tessema et al. 2026).

The same Awash River Basin study noted that wheat experienced reductions of up to 5.0% in crop water demand and 15.6% in irrigation demand, associated with seasonal shifts (Tessema et al. 2026). This crop-specific divergence is an important nuance to acknowledge the maize-focused analysis in the present study may not generalize to all crops in the Kulfo watershed. The larger relative increase in NIR (43.3%) compared to CWR (15.2%) reflects the compounding effect of reduced effective rainfall and increased evaporative demand, which jointly amplify the supplemental irrigation requirement beyond what would be expected from temperature-driven increases in crop water demand alone.

4. Discussion

4.1 Integrated climate–soil–irrigation assessment

The principal contribution of this study is the integration of bias-adjusted climate projections, depth-resolved soil-moisture modelling, explainable machine learning, and crop-water accounting within a common framework. Rather than treating climate forcing and agricultural water demand as independent problems, the framework links changes in precipitation and temperature to soil-water dynamics and subsequently to irrigation requirements.

The projected decline in soil moisture under stronger climate forcing occurred alongside increases in crop-water and irrigation requirements. This combination is particularly relevant to irrigation-dependent agriculture because declining soil-water availability can increase the need for supplemental irrigation during crop growth. The depth-dependent response further demonstrates that soil moisture should not necessarily be represented by a single layer. The stronger relative response near the surface suggests greater sensitivity to short-term rainfall variability and atmospheric demand, whereas deeper layers retain greater hydrological memory.

The integration of recursive hindcasting provides an important bridge between model development and future simulation. By demonstrating that predictive skill remains satisfactory when predicted soil moisture is used as a lagged input, the recursive hindcast establishes the credibility of the future scenario simulations. This approach addresses a critical gap in many machine-learning-based soil moisture studies, where models are evaluated only under one-step prediction conditions that do not reflect operational forecasting constraints.

4.2 Climate-model correction and uncertainty

This study distinguishes three concepts explicitly: uncertainty in the climate-model ensemble, uncertainty introduced by the bias-adjustment method, and uncertainty associated with the machine-learning and recursive forecasting framework. These were not combined into a single confidence statement because a formal uncertainty-propagation analysis was not performed. All 18 GCMs were weighted equally in the multi-model mean. This avoids overconfidence in any single model but does not account for model interdependence.

QM addresses distributional discrepancies, while RF residual correction can represent remaining nonlinear systematic relationships. The QM–RF framework reduced precipitation RMSE by an average of 18.1% relative to QM alone, with the largest improvement for CMCC-ESM2 (21.6%). However, statistical bias adjustment does not eliminate structural GCM uncertainty, and

historical performance does not guarantee future predictive skill. A 2026 study evaluating 18 bias correction methods concluded that “it is important to select methods suited to the specific conditions and intended use, to improve the reliability of future climate and hydrological projections” {Citation}(Bodjrènou et al., 2026). Retaining multiple GCMs and reporting their spread therefore provides a more defensible basis for future scenario assessment than relying on a single historically best-performing model. The 10th–90th percentile range reported here represents inter-model spread and should not be interpreted as a formal confidence interval.

The distinction between distributional correction and residual correction is important for interpreting the QM–RF results. QM corrects the systematic differences in the probability distribution of climate variables, but it cannot correct conditional biases that depend on the state of other variables or on temporal sequences. The RF residual correction addresses these conditional biases by using the QM-corrected value, the raw GCM value, day-of-year, and lagged residuals as predictors. This two-stage approach is particularly valuable for precipitation, where the occurrence and intensity of wet days are critical for soil moisture recharge.

4.3 Depth-dependent soil-moisture response

The stronger projected response in shallow soil is physically consistent with direct exposure to rainfall variability and atmospheric evaporative demand. Deeper soil moisture is influenced by infiltration, redistribution, storage, drainage, and delayed hydrological responses, providing partial buffering against short-term climate variability. Nevertheless, reduced soil moisture at 30–40 cm remains important for crops whose roots extend into these layers. The agricultural significance ultimately depends on rooting depth, soil hydraulic properties, crop water uptake, and allowable depletion.

The depth-dependent SHAP results provide additional insight into the mechanisms driving these differences. The greater contribution of antecedent soil moisture at deeper layers reflects the longer memory of subsurface hydrological processes. Precipitation influences shallow layers directly through infiltration, but its effect on deeper layers is mediated by soil hydraulic properties and antecedent moisture conditions. Temperature influences soil moisture through evapotranspiration, but its effect is modulated by vegetation cover and radiation, which were not explicitly represented in the predictor set. The, R^2 is reported as the squared Pearson correlation coefficient, not the coefficient of determination.

4.4 Implications for agricultural water management

The projected increase in crop-water and irrigation requirements under stronger climate forcing suggests additional pressure on agricultural water resources. Potential adaptation measures include improved irrigation application efficiency, soil-water conservation, mulching, improved irrigation scheduling, water harvesting, drought-tolerant cultivars, and adjustment of crop calendars.

The suitability and effectiveness of these measures depend on local water availability, crop economics, irrigation infrastructure, and farmer capacity. The projected irrigation requirements should therefore be interpreted as scenario-dependent water-balance estimates rather than direct predictions of future water withdrawals. The finding that NIR increases more rapidly than CWR (43.3% vs 15.2% under SSP5-8.5) suggests that adaptation strategies focused solely on reducing crop water demand may be insufficient; measures that enhance soil water storage and reduce non-beneficial evaporation may be equally important. In addition, the CWR and NIR results are maize-specific and should not be treated as watershed-wide totals without crop-specific parameterization.

4.5 Explainability and model interpretation

SHAP analysis provides a useful framework for identifying predictors contributing to soil-moisture predictions and for comparing attribution patterns across depths. The greater contribution of antecedent soil moisture at deeper layers is consistent with greater subsurface hydrological persistence, whereas precipitation is expected to have stronger short-term influence in shallow layers. Because predictors can be physically and statistically correlated, SHAP contributions should be interpreted as model attribution rather than evidence of causal relationships.

The depth-dependent shift in predictor importance has practical implications for model development. If precipitation is the dominant predictor at shallow depths, then accurate precipitation forecasts are critical for shallow soil moisture prediction. Conversely, if lagged soil moisture dominates at deeper layers, then the recursive forecasting approach becomes more important, and errors in antecedent predictions may propagate more strongly. The SHAP results therefore support the use of recursive hindcasting as a necessary evaluation step for future scenario simulation.

4.6 Uncertainty, limitations, and future research

Several sources of uncertainty affect the projected soil-moisture and irrigation changes. Climate uncertainty arises from differences among CMIP6 models and emissions pathways, while bias-adjustment uncertainty is associated with the statistical correction method and calibration period.

Machine-learning uncertainty arises from model structure, predictor selection, hyperparameter configuration, and recursive error propagation. The observational period of 2006–2014 is relatively short and may not capture the full range of hydroclimatic variability or rare extremes. This short record also limits the ability of machine-learning models to generalize to conditions outside the training distribution, particularly for extreme wet or dry years, and may reduce the robustness of bias-correction relationships when extrapolated to future climates. The available observations may also not fully represent spatial variability across the watershed.

The predictor set is dominated by precipitation and temperature and does not explicitly represent radiation, humidity, wind, vegetation dynamics, or detailed soil hydraulic properties. Recursive forecasting introduces an additional source of uncertainty because small prediction errors can propagate through successive time steps. Previous work on autoregressive soil moisture prediction has noted that model uncertainty gradually accumulates with prediction time, although it can remain within acceptable bounds over a 120-day forecast. The 2026 Euler-Net study similarly demonstrated that discrete-time tendency learning can mitigate error accumulation in long-term recursive forecasting, achieving a median R^2 of 0.74 while using an order of magnitude fewer parameters (Kang et al. 2026). Although the recursive hindcast in the present study provides an important reliability assessment, longer hindcast periods would provide stronger evidence regarding long-term error accumulation.

Finally, irrigation estimates depend on crop coefficients, rooting depth, soil-water thresholds, effective rainfall, drainage, runoff, and irrigation efficiency. Future studies should incorporate longer and spatially distributed soil-moisture observations, explicit ensemble uncertainty, physically constrained learning, and crop-specific root-zone water uptake. The integration of remote sensing data, particularly soil moisture retrievals from Sentinel-1 or SMAP, could help address the spatial limitations of the current point-scale observations and provide a basis for validating the depth-resolved predictions across the watershed.

5. Conclusions

This study developed an integrated framework combining bias-adjusted CMIP6 climate simulations, multi-depth machine learning, explainable artificial intelligence, recursive hindcasting, and root-zone water-balance modelling to assess climate-driven changes in soil moisture and irrigation requirements in the Kulfo watershed, southern Ethiopia.

The 18 evaluated CMIP6 models exhibited substantial differences in their historical representation of precipitation and temperature. Following bias adjustment, CMCC-ESM2 achieved the highest precipitation performance index, while NorESM2-MM achieved the highest indices for maximum and minimum temperature. These rankings represent historical statistical agreement rather than future model certainty. QM–RF reduced precipitation RMSE by an average of 18.1% relative to QM alone.

The machine-learning models reproduced the principal temporal variability of soil moisture at 10, 20, 30, and 40 cm. CatBoost achieved the strongest independent-test performance at 40 cm, while HistGB was best at 20 cm. Recursive hindcast results demonstrated that predictive skill remained satisfactory when predicted soil moisture was used as a lagged input. SHAP analysis indicated that precipitation and antecedent soil moisture were important predictors, with their relative contributions varying across soil depths.

Future simulations indicated progressively greater soil-moisture depletion with increasing radiative forcing. Under SSP5-8.5, annual mean soil moisture decreased by approximately 29%, 27%, 24%, and 21% at 10, 20, 30, and 40 cm, respectively, relative to the historical baseline. At the same time, crop water requirement increased from 620 mm during the historical baseline to 714 mm during 2071–2100, while net irrigation requirement increased from 210 to 301 mm. These crop-water results are specific to maize and should not be generalized to all crops in the watershed without crop-specific parameterization.

The simultaneous decline in soil-water availability and increase in crop-water demand suggests increasing pressure on irrigation resources under stronger climate forcing. However, these projections remain conditional on climate-model selection, bias-adjustment methodology, recursive machine-learning behavior, observational limitations, and crop-water-balance assumptions. The irrigation results should be interpreted as scenario-dependent water-balance estimates rather than deterministic forecasts of future water withdrawals.

Overall, the study demonstrates the value of integrating climate projections, depth-resolved soil-moisture modelling, explainable machine learning, and crop-water accounting for climate-sensitive irrigation assessment**.**

Data availability

The observational precipitation, temperature, and field soil-moisture data were obtained from the Arba Minch University monitoring system for 2006–2014. CMIP6 simulations are publicly available through the Earth System Grid Federation. Processed datasets and machine-learning code generated during the study are available from the corresponding author upon reasonable request, subject to applicable data-sharing restrictions.

Author contributions

B.T.Y.: Conceptualization, methodology, software, data curation, formal analysis, visualization, investigation, writing—original draft, and project administration. D.D.D.: Supervision, methodology, investigation, resources, and writing—review and editing. H.M.A.: Validation, investigation, data curation, and writing—review and editing. D.W.G.: Validation, investigation, data curation, and writing—review and editing.

Funding

This research received no specific grant from any funding agency in the public, commercial, or not-for-profit sectors. The study was conducted as part of the authors' academic research activities at Arba Minch University.

Declaration of competing interests

The authors declare that they have no known financial or personal relationships that could have influenced the work reported in this manuscript.

Acknowledgements

The authors thank Arba Minch University for providing access to the available meteorological and soil-moisture observations. The authors also acknowledge the international climate-modelling community for developing and distributing CMIP6 climate simulations through the Earth System Grid Federation.

Declarations

Ethical Approval

Not applicable. This study used secondary hydro-climatic datasets and did not involve human participants, animals, or experimental procedures requiring ethical approval.

Consent to Participate

Not applicable. No human participants were involved in this study.

Consent to Publish

Not applicable. This manuscript does not contain identifiable personal information requiring consent for publication.

References

Alahmad T, Neményi M, Nyéki A (2026) Explainable XGBoost-based models of root-zone soil moisture profiling using coupled Sentinel-2 and IoT data in loam and silt loam soil. Discov Appl Sci 8:672. https://doi.org/10.1007/s42452-026-08673-3

Alemu MG, Serur AB, Wudineh FA, Beker BA (2026) AI-driven projection of seasonal agricultural drought using CMIP6 and remote sensing data in Borena Zone, Southern Ethiopia. Sci Rep 16:29119. https://doi.org/10.1038/s41598-026-55341-y

Ashagre HM, Goshime DW, Yersaw BT, Walle MA (2026) Machine learning and bias corrected CMIP6 for improved streamflow prediction in the data-scarce Kulfo river, Ethiopia. Discov Sustain. https://doi.org/10.1007/s43621-026-04724-2

Ayugi B, Shilenje ZW, Babaousmail H, et al (2021) Projected Changes in Meteorological Drought Over East Africa Inferred from Bias-Adjusted CMIP6 Models

Babaousmail H, Hou R, Ayugi B, et al (2021) Evaluation of the Performance of CMIP6 Models in Reproducing Rainfall Patterns over North Africa. Atmosphere 12:475. https://doi.org/10.3390/atmos12040475

Berg A, Sheffield J (2018) Climate Change and Drought: the Soil Moisture Perspective. Curr Clim Change Rep 4:180–191. https://doi.org/10.1007/s40641-018-0095-0

Bischof B, Klotz D, Gupta HV, et al (2026) Exploring soil moisture dynamics and variability across scales and geological settings using gaussian mixture-long short-term memory networks. J Hydrol 664:134364. https://doi.org/10.1016/j.jhydrol.2025.134364

Bitew AB, Minale AS (2025) Evaluation of past and future trends of temperature and rainfall under CMIP6 scenarios in the Ayehu watershed, Upper Blue Nile Basin, Ethiopia. J Water Clim Change 16:2153–2184. https://doi.org/10.2166/wcc.2025.032

784 Bodjrènou R, Sintondji LO, Ahamidé B, et al (2026) Challenges in reliable bias correction of hydro-climatic
785 and energy data: Towards a reconstruction of datasets. Int J Appl Earth Obs Geoinformation
786 150:105362. https://doi.org/10.1016/j.jag.2026.105362

787 Bokke AS, Gerasu TS, Demissie TA, et al (2026a) Climate change on crop water requirements, irrigation,
788 and scheduling in Jimma, Ethiopia: using CMIP6. Water Sci 40:2. https://doi.org/10.1007/s44533-
789 025-00010-8

790 Bokke AS, Gerasu TS, Demissie TA, et al (2026b) Climate change on crop water requirements, irrigation,
791 and scheduling in Jimma, Ethiopia: using CMIP6. Water Sci 40:2. https://doi.org/10.1007/s44533-
792 025-00010-8

793 Bradford JB, Schlaepfer DR, Lauenroth WK, et al (2017) Future soil moisture and temperature extremes
794 imply expanding suitability for rainfed agriculture in temperate drylands. Sci Rep 7:12923.
795 https://doi.org/10.1038/s41598-017-13165-x

796 Chanie FM (2025) Evaluation of CMIP6 model performance and future climate projections over the Genale
797 dawa river basin, Ethiopia. Sci Rep 16:361. https://doi.org/10.1038/s41598-025-29498-x

798 Chinasho A, Bedadi B, Lemma T, et al (2025) Analysis of past and future temperature variability and change
799 in Southern Ethiopia. Int J Clim Change Strateg Manag 17:397–421.
800 https://doi.org/10.1108/IJCCSM-04-2023-0052

801 Dembélé M, Schaefli B, Van De Giesen N, Mariéthoz G (2020) Suitability of 17 gridded rainfall and
802 temperature datasets for large-scale hydrological modelling in West Africa. Hydrol Earth Syst Sci
803 24:5379–5406. https://doi.org/10.5194/hess-24-5379-2020

804 Demir MS (2026) Multi-Depth Soil Moisture Prediction Using Machine Learning Across Türkiye's Diverse
805 Environments. Tarım Bilim Derg 32:423–438. https://doi.org/10.15832/ankutbd.1809955

806 Demissie T, Diro GT, Duku C, et al (2025) Current and projected changes in climate extremes and agro-
807 climatic zones over East Africa. Theor Appl Climatol 156:179. https://doi.org/10.1007/s00704-025-
808 05405-2

809 Dheeraj Bhima Raut, Vaibhav Misal, Rajeshwari Pangarkar, et al (2025) Nonlinear Soil Moisture Retrieval
810 from Sentinel-1 SAR Using Ensemble Machine Learning. Int J Sci Res Sci Technol 12:616–626.
811 https://doi.org/10.32628/IJSRST25126387

812 Dong J, Xia W, Hao H, et al (2026) Unraveling meteorological contributions and lagged effects on multi-
813 depth soil moisture prediction using Transformer-SHAP framework. J Hydrol 679:136349.
814 https://doi.org/10.1016/j.jhydrol.2026.136349

815 Doshi SC, Lohmann G, Ionita M, Michele CD (2026) Continental-scale bias correction and random forest
816 downscaling of CMIP6 precipitation across Europe. Geocarto Int 41:2657618.
817 https://doi.org/10.1080/10106049.2026.2657618

818 Enyew FB, Sahlu D, Tarekegn GB, et al (2024) Performance Evaluation of CMIP6 Climate Model
819 Projections for Precipitation and Temperature in the Upper Blue Nile Basin, Ethiopia. Climate
820 12:169. https://doi.org/10.3390/cli12110169

821 Erenso KT, Mohammed AK, Lohani TK (2026) Bias-corrected CMIP6 ensemble projections of temperature
822 extremes and precipitation regimes in the Omo-Kuraz Watershed, Ethiopia: Implications for water
823 security. Environ Chall 25:101649. https://doi.org/10.1016/j.envc.2026.101649

824 Galvincio JD, De Queiroga Miranda R, Da Luz GG (2024) Use of Soil Moisture as an Indicator of Climate
825 Change in the SUPer System. Hydrology 11:65. https://doi.org/10.3390/hydrology11050065

826 Gao Y, Zhao T, Wang J, et al (2026) High-precision root zone soil moisture inversion for arid cotton fields
827 using UAV-meteorological-physiological multi-source data fusion. Agric Water Manag 332:110513.
828 https://doi.org/10.1016/j.agwat.2026.110513

829 Greiser C, Hederová L, Vico G, et al (2024) Higher soil moisture increases microclimate temperature
830 buffering in temperate broadleaf forests. Agric For Meteorol 345:109828.
831 https://doi.org/10.1016/j.agrformet.2023.109828

832 Guyasa AK, Danrong Z, Guan Y, et al (2026) Multi-criteria hybrid-based bias correction selection, and
833 machine learning ensemble modeling to improve extreme climate event projections in the Tendaho
834 Catchment, Ethiopia. Theor Appl Climatol 157:3. https://doi.org/10.1007/s00704-025-05908-y

835 He L, Zhang C, Tang P, et al (2026) Enhancing soil moisture prediction via a physics-informed xLSTM with
836 multi-variate temporal dynamics. Eng Appl Comput Fluid Mech 20:2678125.
837 https://doi.org/10.1080/19942060.2026.2678125

838 Huang S, Zhang X, Chen N, et al (2022) A Novel Fusion Method for Generating Surface Soil Moisture Data
839 With High Accuracy, High Spatial Resolution, and High Spatio-Temporal Continuity. Water Resour
840 Res 58:e2021WR030827. https://doi.org/10.1029/2021WR030827

841 Jimma TB, Demissie T, Diro GT, et al (2023) Spatiotemporal variability of soil moisture over Ethiopia and
842 its teleconnections with remote and local drivers. Theor Appl Climatol 151:1911–1929.
843 https://doi.org/10.1007/s00704-022-04335-7

844 Kang W, Liu P, Chen M, et al (2026) Euler-Net: A Tendency Learning Framework for Robust Long-Term
845 Soil Moisture Forecasting

846 Lai EN, Wang-Erlandsson L, Virkki V, et al (2023) Root zone soil moisture in over 25 % of global land
847 permanently beyond pre-industrial variability as early as 2050 without climate policy. Hydrol Earth
848 Syst Sci 27:3999–4018. https://doi.org/10.5194/hess-27-3999-2023

849 Lamichhane M, Mehan S, Mankin KR (2025a) Multi-layer root zone soil moisture estimation using field and
850 remote sensing data fusion with machine learning in semi-arid croplands. Vadose Zone J 24:e70047.
851 https://doi.org/10.1002/vzj2.70047

852 Lamichhane M, Mehan S, Mankin KR (2025b) Soil Moisture Prediction Using Remote Sensing and Machine
853 Learning Algorithms: A Review on Progress, Challenges, and Opportunities. Remote Sens 17:2397.
854 https://doi.org/10.3390/rs17142397

855 Legass AM, Alamirew T, Gebrehiwot SG, et al (2025a) Spatiotemporal climate change projection and trend
856 analysis using selected downscaled CMIP6 models for water action over awash River Basin,
857 Ethiopia. Environ Chall 18:101059. https://doi.org/10.1016/j.envc.2024.101059

858 Legass AM, Alamirew T, Gebrehiwot SG, et al (2025b) Spatiotemporal climate change projection and trend
859 analysis using selected downscaled CMIP6 models for water action over awash River Basin,
860 Ethiopia. Environ Chall 18:101059. https://doi.org/10.1016/j.envc.2024.101059

861 Lesinger K, Tian D (2025a) Skillful subseasonal soil moisture drought forecasts with deep learning-dynamic
862 models. Nat Commun 16:7461. https://doi.org/10.1038/s41467-025-62761-3

Lesinger K, Tian D (2025b) Skillful subseasonal soil moisture drought forecasts with deep learning-dynamic models. Nat Commun 16:7461. https://doi.org/10.1038/s41467-025-62761-3

Li Q, Xiao Q, Zhang C, et al (2024a) Improving global soil moisture prediction through cluster-averaged sampling strategy. Geoderma 449:116999. https://doi.org/10.1016/j.geoderma.2024.116999

Li Q, Xiao Q, Zhang C, et al (2024b) Improving global soil moisture prediction through cluster-averaged sampling strategy. Geoderma 449:116999. https://doi.org/10.1016/j.geoderma.2024.116999

Liu J, Chen Y, Liu X, et al (2025) Soil hydrological processes and drought response of typical vegetation in arid regions under long-term climate patterns. J Hydrol Reg Stud 62:102919. https://doi.org/10.1016/j.ejrh.2025.102919

Liu Y, Ao C, Zeng W, et al (2026) Innovative synergistic optimization of drip irrigation and subsurface drainage for alleviating salinization and improving crop productivity in arid irrigation district. Agric Water Manag 323:110089. https://doi.org/10.1016/j.agwat.2025.110089

Mohammed JA, Almazroui M, Rashid IU, et al (2027) Performance evaluation of CMIP6 GCMs and projection of precipitation extremes over the Jemma sub-basin, Upper Blue Nile basin of Ethiopia. Phys Chem Earth Parts ABC 145:104821. https://doi.org/10.1016/j.pce.2026.104821

Qin T, Feng J, Zhang X, et al (2023) Continued decline of global soil moisture content, with obvious soil stratification and regional difference. Sci Total Environ 864:160982. https://doi.org/10.1016/j.scitotenv.2022.160982

Sa'adi Z, Alias NE, Yusop Z, et al (2024) Application of relative importance metrics for CMIP6 models selection in projecting basin-scale rainfall over Johor River basin, Malaysia. Sci Total Environ 912:169187. https://doi.org/10.1016/j.scitotenv.2023.169187

Shenkut A, Alemayehu G, Tesfaye K, et al (2025) Evaluation of CMIP6 GCM Performance in Simulating Historical Rainfall and Temperature Climatology of the Tana and North Gojjam Sub-Basins in the Upper Blue Nile Basin, Northwestern Ethiopia. Int J Climatol 45:e70059. https://doi.org/10.1002/joc.70059

Tefera GW, Ray RL, Jackson R, et al (2026) Integrating machine learning models with ground sensors to enhance soil moisture prediction in agroecosystems of Texas. Comput Electron Agric 242:111358. https://doi.org/10.1016/j.compag.2025.111358

Teshome FT, Bayabil HK, Schaffer B, et al (2024) Improving soil moisture prediction with deep learning and machine learning models. Comput Electron Agric 226:109414. https://doi.org/10.1016/j.compag.2024.109414

Tessema RS, Kidanewolde BB, Chukalla AD, Van Griensven A (2026) Projections of Sugarcane Water Productivity and Irrigation Use Under Climate Change Using CMIP6 and SWAT+. Earth Syst Environ 10:11089–11110. https://doi.org/10.1007/s41748-026-01206-3

Tsegaye Tadase A, Tekile AK (2026) XGBoost-based bias correction of CMIP6 precipitation in the Wabi Shebelle Basin, Ethiopia: a comparative study with empirical quantile mapping. J Water Clim Change 17:683–700. https://doi.org/10.2166/wcc.2026.103

Wang Y, Shi L, Hu Y, et al (2024) A comprehensive study of deep learning for soil moisture prediction. Hydrol Earth Syst Sci 28:917–943. https://doi.org/10.5194/hess-28-917-2024

Wu Q, Zhu Z, Ma J, et al (2026) High-resolution soil moisture retrieval in heterogeneous terrain: A comparison of ensemble learning approaches using landsat 8/9. J Hydrol Reg Stud 64:103236. https://doi.org/10.1016/j.ejrh.2026.103236

Yin H, Bista P, Ghimire R, et al (2026) Unraveling soil moisture dynamics with dual-scale interpretable machine learning: Cover cropping and irrigation insights in semi-arid agriculture. Vadose Zone J 25:e70077. https://doi.org/10.1002/vzj2.70077

Zhang L, Zhang Y, Ji W, Xue Z (2025a) Stacking Gaussian Process Regression for Soil Moisture Estimation Over the Continental U.S. IEEE Access 13:97597–97608. https://doi.org/10.1109/ACCESS.2025.3576157

Zhang Z, Wang J, Ding J, et al (2025b) Soil moisture retrieval and spatiotemporal variation analysis based on deep learning. Agric Water Manag 317:109622. https://doi.org/10.1016/j.agwat.2025.109622